JOURNAL OF SOLID STATE CHEMISTRY 106, 461–475 (1993)

A 3D Model for the Diffuse Scattering in Cubic Stabilized Zirconias

T. R. WELBERRY, B. D. BUTLER, J. G. THOMPSON, AND R. L. WITHERS

Research School of Chemistry, Australian National University, GPO Box 4, Canberra City, ACT 0200, Australia

Received October 5, 1992; in revised form February 15, 1993; accepted February 19, 1993

We describe the development of a three-dimensional (3D) model which provides a simple explanation of virtually all the features that occur in the complex diffuse X-ray diffraction patterns of an yttria-stabilized cubic zirconia. The model consists of two stages: a scheme for ordering the oxygen vacancies, followed by the relaxation of the cations around these vacancies. Monte Carlo simulation is used in both these stages, followed by direct computation of the diffraction patterns from the resulting lattice realizations. The model which at present best fits the observed scattering patterns is one in which the oxygen vacancies order in such a way as to avoid nearest-neighbor $\frac{1}{2}\langle 1\ 0\ 0\rangle$ pairs, next-nearest $\frac{1}{2}\langle 1\ 1\ 0\rangle$ pairs, and third-nearest $\frac{1}{2}\langle 1\ 1\ 1\rangle$ pairs across empty cubes of oxygens, but allows third-nearest $\frac{1}{2}\langle 1\ 1\ 1\rangle$ pairs across cubes of oxygens containing the cations. These vacancy pairs, which essentially provide octahedral coordination of the enclosed cation, are therefore present almost entirely as either single isolated octahedra or neighboring $\langle 1\ 1\ 0\rangle$ pairs of octahedra. A comparison of the diffuse patterns with those from a calcia-stabilized zirconia is made. © 1993 Academic Press, Inc.

1. Introduction

In a previous paper (*1*) we reported the experimental measurement and preliminary interpretation of the complex diffuse X-ray scattering patterns that were obtained from an yttria-stabilized cubic zirconia (Y-CSZ) of composition $Zr_{0.61}\ Y_{0.39}\ O_{1.805}$ (space group $Fm3m$, $a = 5.175$ Å). In Figs. 1a–1c we reproduce for convenience the $0.1c^*$ and $0.5c^*$ sections of the observed data and also show more recently collected data obtained from the h,k,l, $(h + k + l) = 0.5$ reciprocal section. Of all the recorded sections, these latter two appear to be the most informative. For comparison we also show recently recorded data from the same reciprocal sections of a calcia-stabilized zirconia, composition $Zr_{0.875}\ Ca_{0.125}\ O_{1.875}$.

Our approach in trying to understand these complex diffraction patterns in CSZs is dictated by the simple fact that for Y-CSZ cation-ordering is not directly observable in the diffraction experiment, because of the similarity of the scattering powers of Y and Zr. Even for Ca-CSZs the diffraction patterns are so similar in form to those for Y-CSZs that it is clear that, for this system too, the direct diffraction-contrast between the cations is still a relatively unimportant component of the scattering. The Laue monotonic scattering for the oxygen/vacancy disorder may be shown by simple calculation to be similarly relatively unimportant, and so we may therefore assume that the diffraction patterns arise almost entirely from cation displacements due to strains induced by the disorder. It is the aim of the present work to formulate a model for these strain fields from which inferences can be made regarding the distribution of oxygen vacancies and of the two types of cation. To do this we utilize a two-stage process in which a distribution of oxygen vacancies is first set-up and then subsequently the cations are allowed to relax

0022-4596/93 $5.00
Copyright © 1993 by Academic Press, Inc.
All rights of reproduction in any form reserved.

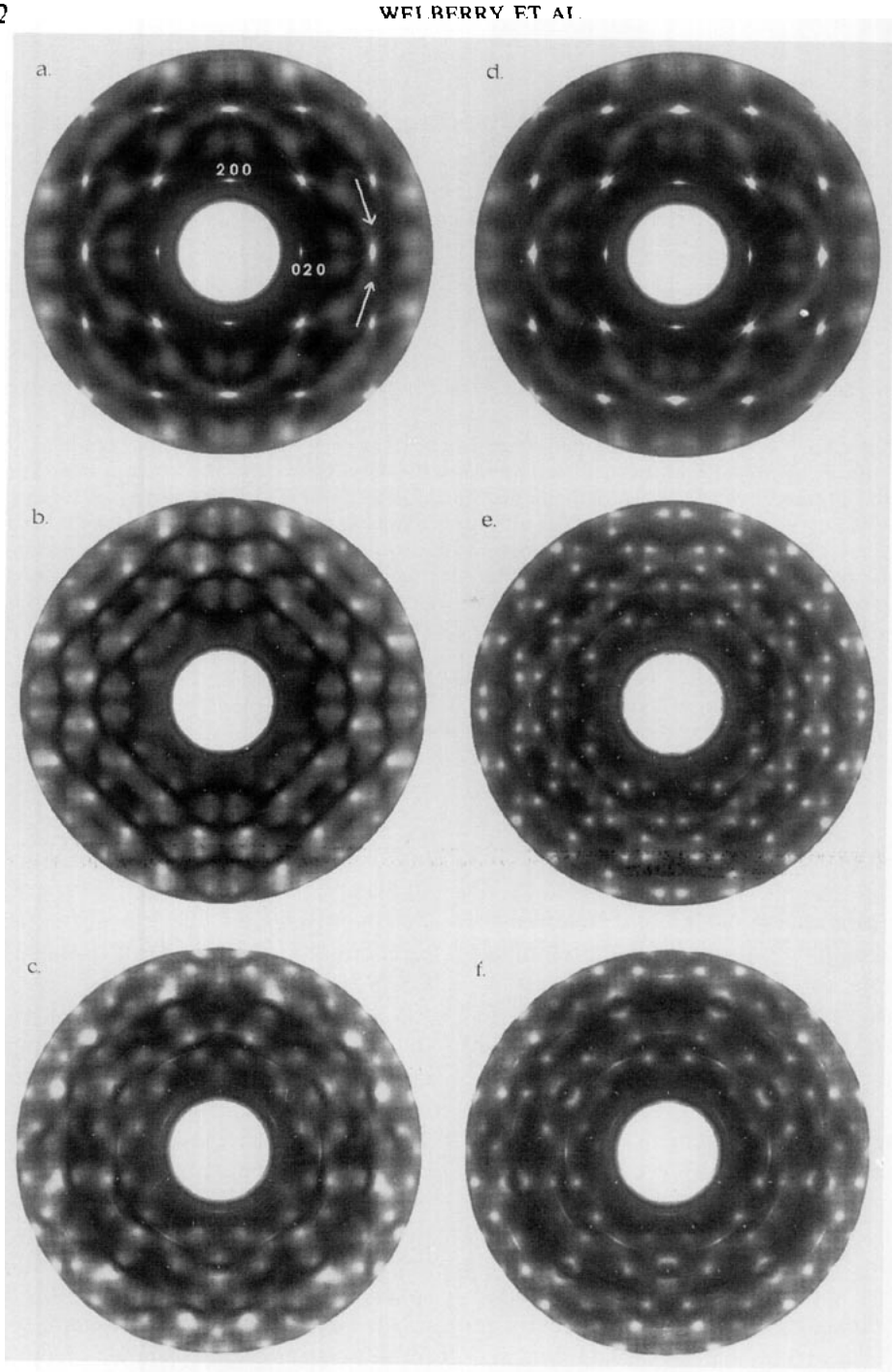

FIG. 1. Sections of the 3D diffuse X-ray diffraction patterns of yttria-stabilized cubic zirconia (a, b, c) and calcia-stabilized cubic zirconia (d, e, f). The sections are: (a, d), $h,k,$ 0.1; (b,e), $h,k,0.5$; (a,d), h,k,l $(h + k + l) = 0.5$. The maximum value of the diffraction angle shown is ~117° of 2θ. The sections were recorded using a position sensitive linear detector. The digital data are displayed as gray-scale images to facilitate visual comparison with the calculated patterns of Fig. 8.

around them. The diffraction pattern of such a distribution may then be computed for comparison with the observed X-ray diffraction patterns. We do not wish to imply that this describes the sequence of events in the formation of CSZs in nature, for it is more likely that ordering of the cations drives the ordering of the vacancies. It is simply a means to an end. By this means we are able to investigate how different distributions of vacancies affect the diffraction patterns, and similarly how different ways in which the cations may relax around the vacancies also affect the diffraction patterns.

In our previous study it was shown that most of the characteristic features of the observed diffraction pattern could be reproduced by a simple model, representing one two-dimensional (2D) layer of the structure, in which local distortions were imposed according to the rule that the distance between neighboring cations along ⟨110⟩ directions was increased if either of the two bridging oxygens was missing and relatively decreased if both were present. These *size-effect*-like distortions give rise to a number of very characteristic features in the diffraction patterns. The most important of these is a set of dark lines (actually planes normal to ⟨110⟩). This has been attributed (*2*) to the correlations that are induced, by the local distortions, between the displacements of cations running in chains along the ⟨110⟩ directions. A second prominent feature of the patterns is the *bow-tie*-shaped regions of scattering, present in some reciprocal sections. These have been found to be closely associated with the same correlated displacements of cations (*2*). A particularly important consequence of these *bow-tie* features is that their polarity or azimuthal variation of intensity indicates that a local expansion of the lattice along [1 1 0] say is accompanied by a contraction along [1 −1 0]. For this condition to be satisfied for the proposed relaxation mechanism, it is necessary that nearest-neighbor ($\frac{1}{2}$⟨1 0 0⟩) oxygen vacancies be avoided. Although the observed scattered intensity is purely displacive in origin, the details of the patterns were found to be very sensitive to the oxygen vacancy ordering scheme. In particular the diffuse peaks that occur in the vicinity of the $\mathbf{G} + \frac{1}{2}\{1\ 1\ 1\}^*$ reciprocal position (where **G** is a reciprocal lattice vector) must result indirectly from short-range ordering of the vacancies.

Although in our previous study much was learned of the origins of the different features of the diffraction patterns using the 2D single-layer model, a completely satisfactory description of the ordering was not forthcoming, and moreover it was unclear how the basic ideas encompassed in the 2D model could be incorporated into a fully 3D one. In the present paper we describe subsequent work in which we have extended the ideas developed in the earlier paper to obtain a 3D model for the vacancy ordering and cation relaxation which can account qualitatively for the observed diffraction patterns. Although the main purpose of this paper is to present a description of this 3D model, the further development of the 2D model provided the crucial clues which led to the 3D model and we first describe these developments. As before, we use Monte Carlo methods to obtain realizations of a model and then directly compute its diffraction pattern using the algorithm developed by Butler and Welberry (*3*), for comparison with the observed patterns.

2. Two-Dimensional Simulations

In our previous paper (*1*) we used a 2D model system as shown in Fig. 2. The main reason for using such a simplified representation of the cubic-stabilized zirconia structure was to reduce, to manageable proportions, the length and complexity of computer simulations. A fully realistic 3D system using interaction potentials sufficiently general to allow exploration of different possible ordering and relaxation schemes, and of a size sufficiently large that

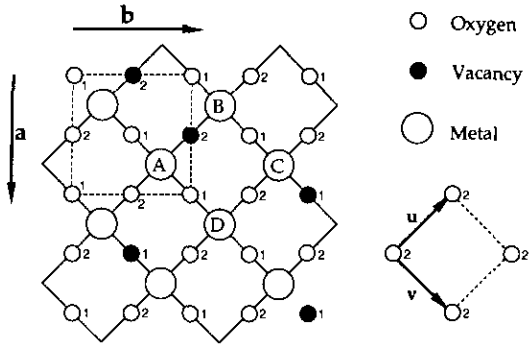

FIG. 2. The 2D model structure used in the simulations.

high-quality diffraction patterns can be computed, requires prohibitive computational resources if more than a few examples are to be produced. Consequently, we continued to use the simplified 2D system in the present work to develop our ideas concerning the origins of different features of the diffraction pattern until such a time that we were confident that these ideas could be transferred into a 3D system. In this section we describe the developments of this 2D model which led to the formulation of a realistic and manageable 3D model.

The 2D model system shown in Fig. 2 may be thought of as representing a single layer of the stabilized zirconia structure. Each small circle represents a superposed pair of oxygen atoms, one above and one below the plane of the cations (depicted by the large circles). A black circle represents a superposed pair of oxygen atom sites, one (at least) of which is a vacancy. We suppose that the intercation site vectors A–B, A–D, etc., have a different length according to whether there is an oxygen vacancy (black circle) between the two sites. This is justified on the grounds that removal of an oxygen will reduce the shielding between the positive charges on the two cations which would therefore tend to move apart. For example in Fig. 2 we assume that A–B would be longer than average while A–D, B–C, D–C, etc. would be shorter than average. The condition that nearest-neighbor ($\frac{1}{2}$[1 0] or $\frac{1}{2}$[0 1]) vacancies are not allowed, guarantees that the displacements in the [1 1] and [1 −1] directions around an atom such as A are out of phase, A–B being longer while A–D is shorter.

In order to apply this distortion we first need to establish the distribution of oxygen vacancies. In our previous paper this ordering was carried out by assigning energies to each of the configurations on the elementary square, a high energy being used to exclude unwanted configurations. We show in Fig. 3a the example G1_B (Fig. 6a of Ref. (*1*)), which we considered to be the most promising of the simulations produced in this earlier work. In this example the Monte Carlo energies that were used not only guaranteed that nearest-neighbor $\frac{1}{2}\langle 1\ 0\rangle$ vacancy pairs were energetically unfavorable, but so were those next-nearest-neighbor ⟨1 1⟩ pairs which included a cation. The features of this pattern which were considered to correspond well to the observed patterns (see Fig. 1b) were:

(i) The dark lines normal to [1 1] and [1 −1].

(ii) The *bow-tie*-shaped features occurring around the positions (0 2), (0 4), (2 0), (4 0), etc.

(iii) The transfer of intensity across the dark lines, the region on the high-angle side is always more intense than that on the low angle side.

(iv) The broad diffuse nature of the patterns, indicating a rather short range of order, other more ordered examples displayed more highly structured diffraction patterns.

On the other hand the feature of this pattern which was evidently quite unsatisfactory was the absence of the diffuse peaks that are present in the $0.5c^*$ section of the observed data. These are seen (Fig. 1b) to occur in pairs at the extremities of the bow-tie-shaped features, but also along rows in the [1 1] and [1 −1] directions as asymmetric pairs straddling the dark lines. In the simulation pattern, Fig. 3a, there is a line of reduced intensity at this position, indicated by the white arrows. In order to see what

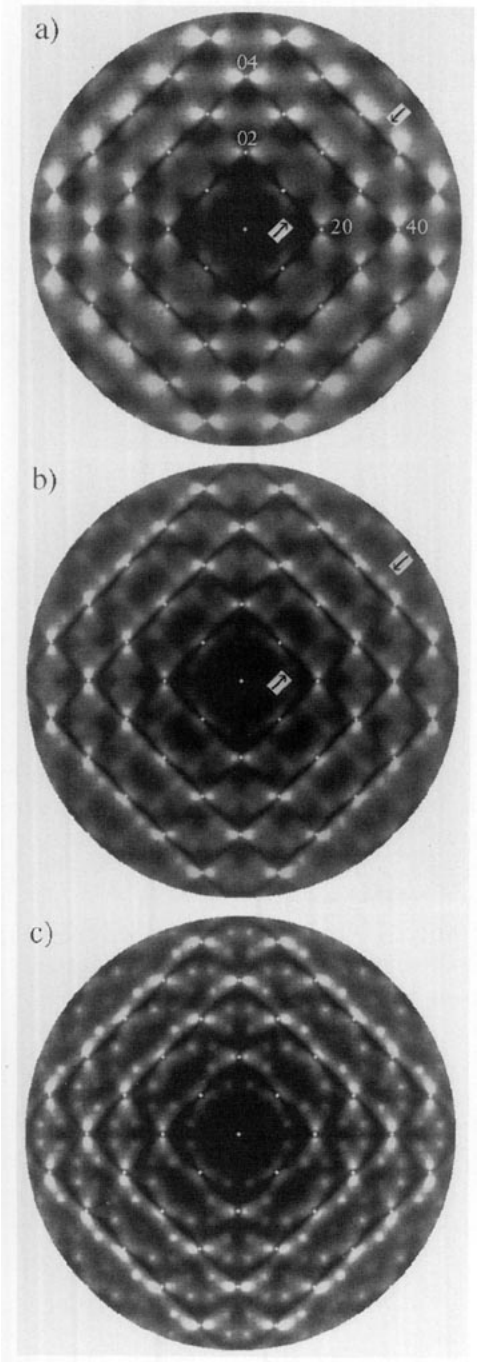

FIG. 3. Diffraction patterns calculated from the 2D model described in the text for the examples whose correlation details are given in Table I. The small white dots mark the positions of integral reciprocal lattice positions.

sort of vacancy ordering scheme might give rise to peaks at this position we first consider this example in more detail.

With reference to Fig. 2 it may be seen that in this 2D model there are two quite distinct sublattices of oxygen sites. The sites labeled "2" are seen to occur between cation sites in the [1 −1] direction (e.g., between A and B), and hence only influence the atomic displacements in this direction. Those labeled "1" on the other hand occur between cation sites in the [1 1] direction (e.g., between A and D) and hence only influence the atomic displacements in this direction. The presence of two sublattices in this 2D model is analogous to the situation in the 3D structure of CSZs in which, although each oxygen site is tetrahedrally coordinated by 4 cation sites, in one half of these the top edge of the tetrahedron points along [1 1 0] while in the other half the top edge points along [1 −1 0].

Since the scattering which occurs in say the [1 −1] direction results only from components of displacements along [1 −1], and that in the [1 1] direction correspondingly from components in the [1 1] direction, to understand the details of the scattering in each of these directions it is necessary to consider the distribution of vacancies on each individual sublattice. (The *bow-tie* features visible in the [1 0] and [0 1] directions result from the strong coupling between the two sublattices caused by the avoidance of nearest-neighbor vacancy pairs.) Let us define axes, **u** and **v**, on the sublattice "2" such that **u** is the vector between adjacent sublattice sites in the [1 −1] direction and **v** is the vector between adjacent sublattice sites in the [1 1] direction. Note that only the components of the cation displacements along [1 −1] are affected by the "2" sublattice.

In Table I we give the values of correlation coefficients $C_{n,m}$ between sites on this sublattice. The index n measures the distance between sites in the **u** direction and m in the **v** direction. $C_{n,m}$ is defined by

$$C_{n,m} = \frac{P_{n,m} - \theta^2}{\theta(1-\theta)}, \tag{1}$$

TABLE I

CORRELATIONS BETWEEN SITES WITHIN ONE SUBLATTICE OF THE OXYGEN ARRAY IN THE 2D SIMULATIONS

	Nearest neighbor along **v**	Second neighbor along **v**	Nearest neighbor along **u**	Second neighbor along **u**	Between two sublattices
Fig. 3a	0.15	−0.02	−0.25	0.07	−0.25
Fig. 3b	−0.20	0.20	0.20	0.00	−0.25
Fig. 3c	−0.20	0.20	0.20	−0.20	−0.25
Fig. 5	−0.20	0.20	0.40	0.16	−0.25

Note. The diffraction patterns of the first three examples are shown in Fig. 3. A portion of the real-space distribution of the last example is shown in Fig. 5. Note that for a vacancy concentration $\theta = 0.2$, the maximum negative correlation that is possible is $-\theta/(1-\theta) = -0.25$.

where $P_{n,m}$ is the probability that sites separated by a vector, n,m are both vacancies, and θ is the overall fraction of vacant sites. A positive value for $C_{n,m}$ indicates that there is a greater than average likelihood for two sites to be both vacant while a negative value indicates a less than average likelihood.

One significant piece of information in this table is that along the **v** direction the nearest-neighbor correlation is positive (0.15). This means that if there is a vacancy in a given [1 −1] row then there will be a more than average likelihood of there being a vacancy at the same position in the neighboring row. This in turn will tend to mean that the displacements of the cations in the two rows will tend to be positively correlated also. This is the reason for the line of low intensity in Fig. 3a. It is consequently clear that the observed patterns must correspond to a negative correlation between such adjacent cation displacements and this in turn implies that there must be a corresponding tendency for the vacancies to be negatively correlated in this direction.

In view of this observation a more sophisticated ordering scheme was set up to allow realizations to be produced in which nearest-neighbor and second-nearest-neighbor correlations along **u** and **v** could be controlled, while at the same time maintaining the strong coupling between the two sublattices, necessary for the exclusion of $\frac{1}{2}\langle 1\ 0\rangle$ vacancy pairs.

2.1. 2D Vacancy Ordering Scheme

We use spin variables, σ_a, to represent the occupancy of a site, a, on the oxygen array, where $\sigma_a = +1$ for a vacancy and $\sigma_a = -1$ for an occupied site. With reference to Fig. 4 for the definition of the site labeling around a given site, we then suppose that the energy of the system is given by,

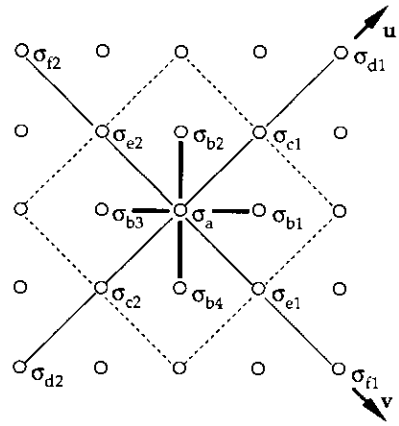

FIG. 4. The local arrangement of variables used in Eq. (2).

$$E = \sum_{\text{sub 1}} \sigma_a [H + J(\sigma_{b1} + \sigma_{b2} + \sigma_{b3} + \sigma_{b4}) + K_1(\sigma_{c1} + \sigma_{c2}) + K_2(\sigma_{d1} + \sigma_{d2}) + K_3(\sigma_{e1} + \sigma_{e2}) + K_4(\sigma_{f1} + \sigma_{f2})] + \sum_{\text{sub 2}} \sigma_a [H + J(\sigma_{b1} + \sigma_{b2} + \sigma_{b3} + \sigma_{b4}) + K_3(\sigma_{c1} + \sigma_{c2}) + K_4(\sigma_{d1} + \sigma_{d2}) + K_1(\sigma_{e1} + \sigma_{e2}) + K_2(\sigma_{f1} + \sigma_{f2})]. \quad (2)$$

The first summation includes all site variables σ_a falling on sublattice "1" and the second those sites falling on sublattice "2." Note that only the K terms link a particular variable with variables in the same sublattice, while the J term provides the coupling to the other sublattice. The H term provides the means of controlling the number of vacancies. Note also that the Ks for the two sublattices have been interchanged to maintain overall square symmetry.

The values of the constants H, J, and K_i necessary to produce lattice realizations with a given correlation structure are in general unknown quantities. Consequently in performing the Monte Carlo simulation we adopted a feed-back mechanism in which, after each cycle of iteration, lattice averages are computed and the values of H, J, and K_i adjusted accordingly. After a large number of Monte Carlo cycles (200 cycles were used in this case) the values of H, J, and K_i settle down to constant values and the lattice averages reach the desired values. This method has been used in other studies (*4*) where it is described in somewhat more detail. A Monte Carlo cycle is defined as that number of individual steps required so that each site is visited once on average.

We show in Figs. 3b and 3c, for comparison with the original Fig. 3a, two examples generated by the new ordering scheme. For each of these examples we have made the correlations in the **v** direction -0.2 for the nearest neighbor and $+0.2$ for the second-nearest neighbor (see Table I also). In the **u** direction the nearest-neighbor correlation is $+0.2$ in each case. The only difference between the two examples is the second-nearest neighbor along **u**. For Fig. 3b the value is 0.0 while for Fig. 3c the value is -0.2.

We see from these figures that the inclusion of the negative nearest-neighbor and positive second-nearest-neighbor correlation along **u** results in intensity being transferred to the positions indicated by the arrows in Fig. 3a. For Fig. 3b this intensity appears as a fairly weak line of intensity, but in Fig. 3c distinct peaks are to be seen. It is worth noting also that the nearest-neighbor correlation along **v** has also changed sign, compared to the example in 3a. If this correlation is maintained as negative, then putting in the new **u** correlations results in intensity appearing midway between the dark lines instead of straddling them.

Figure 3c now shows practically all of the features observed in the real X-ray patterns. It is of course only a 2D model and does not take account of the fact that many of the observed features are present in the $0.5c^*$ section and not the zero-level section that would correspond to a straight projection of the structure. Nevertheless this 2D study provided indispensible clues on how to proceed in formulating a 3D model.

With the small correlation values used to produce Figs. 3b and 3c it is difficult to recognize in the disordered real-space structure any substantive microdomains. In Fig. 5, however, we show a portion of a further example in which the nearest-neighbor correlation along **u** has been increased to 0.4 and the second-neighbor to 0.16. In this realization there are clearly visible microdomains of a structure in which chains of vacancies along [1 1] (or [1 −1]) alternate with chains of complete oxygen strings parallel to them. Two such regions in different orientations have been outlined in the figure. These microdomains are reminiscent of the *pyrochlore* structure (stoichiometry $A_2B_2X_6Y$, or $A_2B_2O_7$ for oxide pyrochlores (*5*)). This fact, together with the fact that in the 3D diffraction patterns the peak features occur in the region of the $\mathbf{G} + \frac{1}{2}\{1\ 1\ 1\}^*$ reciprocal positions (where **G** is a reciprocal

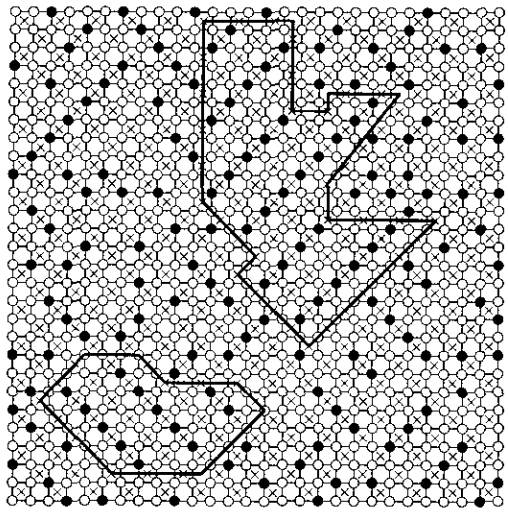

FIG. 5. A small portion of the distribution of oxygen vacancies for the example described in the text in which the nearest-neighbor correlation along **u** is 0.4. With this degree of correlation microdomains of a *pyrochlore*-like structure (indicated) are visible. Open circles represent a superposed pair of oxygen atoms, one above and one below the plane of the cations (indicated by a cross, ×). Black circles represent a superposed pair of oxygen atom sites; one of which is a vacancy.

lattice vector), and that the pyrochlore structure is a fluorite-related structure in which superlattice peaks are present at $\mathbf{G} + \frac{1}{2}\{1\ 1\ 1\}^*$ (6), suggested that a disordered *pyrochlore*-like structure might be a suitable model on which to base the 3D structure. Our initial aim in building a 3D model, therefore, was to generate such a disordered *pyrochlore*-like structure.

3. Three-Dimensional Simulations

Following similar methods to those utilized in 2D, we sought first of all to obtain a model for the oxygen vacancy ordering. Spin variables, $\sigma_{i,j,k}$, were used to represent the oxygen array with $\sigma_{i,j,k} = +1$ to represent a vacancy and $\sigma_{i,j,k} = -1$ to represent an oxygen. (i,j,k) are indexes defining the simple primitive cubic array of O sites. For a complete unit cell of the stabilized zirconia structure an increment of 2 in each of the axial directions is required. Computer simulations were carried out on an array of $64 \times 64 \times 64$ oxygen sites corresponding to $32 \times 32 \times 32$ unit cells. Cyclic boundary conditions were employed. As for the 2D model, two distinct sublattices of oxygens must be considered: those sites for which $i + j + k =$ even (sub 1) and those for which $i + j + k =$ odd (sub 2). The energy of interaction between sites that was used in the Monte Carlo vacancy ordering scheme was then of the form:

$$
\begin{aligned}
E = \sum_{\text{sub1,sub2}} \sigma_{ijk}[H &+ J_1(\sigma_{i-1,j,k} + \sigma_{i+1,j,k} + \sigma_{i,j-1,k} + \sigma_{i,j+1,k} + \sigma_{i,j,k-1} + \sigma_{i,j,k+1}) \\
&+ J_2(\sigma_{i-1,j-1,k} + \sigma_{i+1,j-1,k} + \sigma_{i+1,j+1,k} + \sigma_{i-1,j+1,k} + \sigma_{i-1,j,k-1} + \sigma_{i+1,j,k-1} \\
&+ \sigma_{i+1,j,k+1} + \sigma_{i-1,j,k+1} + \sigma_{i,j-1,k+1} + \sigma_{i,j+1,k-1} + \sigma_{i,j+1,k+1} + \sigma_{i,j-1,k+1})] \\
&+ \sum_{\text{sub1}} \sigma_{ijk}[J_3(\sigma_{i-1,j-1,k-1} + \sigma_{i-1,j+1,k+1} + \sigma_{i+1,j+1,k-1} + \sigma_{i-1,j+1,k-1}) \\
&\quad + J_4(\sigma_{i+1,j+1,k+1} + \sigma_{i+1,j-1,k-1} + \sigma_{i-1,j-1,k+1} + \sigma_{i+1,j-1,k+1})] \\
&+ \sum_{\text{sub2}} \sigma_{ijk}[J_3(\sigma_{i+1,j+1,k+1} + \sigma_{i+1,j-1,k-1} + \sigma_{i-1,j-1,k+1} + \sigma_{i+1,j-1,k+1}) \\
&\quad + J_4(\sigma_{i-1,j-1,k-1} + \sigma_{i-1,j+1,k+1} + \sigma_{i+1,j+1,k-1} + \sigma_{i-1,j+1,k-1})].
\end{aligned}
\tag{3}
$$

J_1 and J_2 are thus seen to represent pair interactions between nearest-neighbor $\frac{1}{2}\langle 1\ 0\ 0\rangle$ and next-nearest $\frac{1}{2}\langle 1\ 1\ 0\rangle$ oxygen sites respectively, while J_3 and J_4 are interactions between third-nearest $\frac{1}{2}\langle 1\ 1\ 1\rangle$ sites. J_3 acts along the body-diagonal of cubes of oxygens which contain a cation, while J_4 acts along the body-diagonal of empty cubes. H is a variable acting only on a single site (analogous to a magnetic field in Ising

TABLE II

VALUES FOR THE CORRELATIONS BETWEEN PAIRS OF OXYGEN SITES SEPARATED BY VARIOUS VECTORS FOR TWO EXAMPLES DESCRIBED IN THE TEXT

Interaction vector		Model 1			Model 2		
		Interaction	Correlation		Interaction	Correlation	
			Attempted	Achieved		Attempted	Achieved
Concentration	H	−0.64			+1.26		
½[1 0 0]	J_1	+2.65	−0.108	−0.105	+2.45	−0.108	−0.106
½[1 1 0]	J_2	+2.58	−1.108	−0.106	+2.37	−0.108	−0.107
½[1 1 1]	J_3	−0.30	0.35	0.349	−4.36	0.35	0.336
½[1 1 1]†	J_4	+2.45	−0.108	−0.106	+2.51	−0.108	0.106
[1 0 0]				−0.054			−0.067
½[2 1 0]				−0.007			0.004
½[2 1 1]				−0.002			0.030
[1 1 0]	J_5			0.177	+1.85	0.00	0.006
½[2 2 1]				−0.067			−0.080
½[2 2 1]†				0.002			0.056
[1 1 1]				−0.054			−0.040

Note. For a vacancy concentration of $\theta = 0.0975$, the maximum negative correlation possible is $-\theta/(1-\theta) = -0.108$ which corresponds to the number of vacancy pairs being zero. Also given are the final values obtained for the interaction parameters, H, J_1, J_2, J_3, J_4, etc. (see Eq. (3)).

spin systems). This is used to control the overall fraction of vacancies present. This Hamiltonian may readily be modified to include longer range terms. To avoid undue complexity in the model and to minimize computer time the minimum number of these has been used to date. For the first of the examples discussed below the Hamiltonian was used as shown, but for the second example one additional interaction was added. Correlations out to the full extent of one unit cell, i.e., ⟨1 1 1⟩ were, however, monitored during the course of the vacancy ordering.

As for the 2D examples the interaction parameters H, J_1, J_2, J_3, J_4 are initially unknown quantities and a similar feed-back mechanism was employed in the Monte Carlo process in order to achieve different desired degrees of ordering between neighboring sites. Monte Carlo iteration was carried out for 300 cycles. Little change in the lattice averages was detected after about 100 cycles.

In Table II we list the interactions that were used and the correlations that were achieved in the two examples which are described below. It should be noted that for ½⟨1 1 1⟩ vectors there are two different interactions, the first (unlabeled) corresponding to interaction, J_3, along the diagonal of a cube of oxygen sites containing a cation; the second (indicated by †) along the diagonal of an empty cube. Similarly, there are two distinct ½⟨2 2 1⟩ vectors for which different correlation values are obtained.

Imposing the condition that vacancy pairs are avoided completely on all nearest-neighbor ½⟨1 0 0⟩, all second-nearest ½⟨1 1 0⟩, and those third-nearest ½⟨1 1 1⟩† neighbor pairs which span empty cubes, a pyrochlore-like structure can be produced simply by having a positive interaction between third-nearest-neighbor pairs in cubes containing a cation site. With a value of 0.35 for this correlation distinct pyrochlore-like regions can be seen in realizations. In Fig. 6a we show a plot of two consecutive layers of oxygen sites from such a realization. The second layer is set slightly up and to the right of the first, so

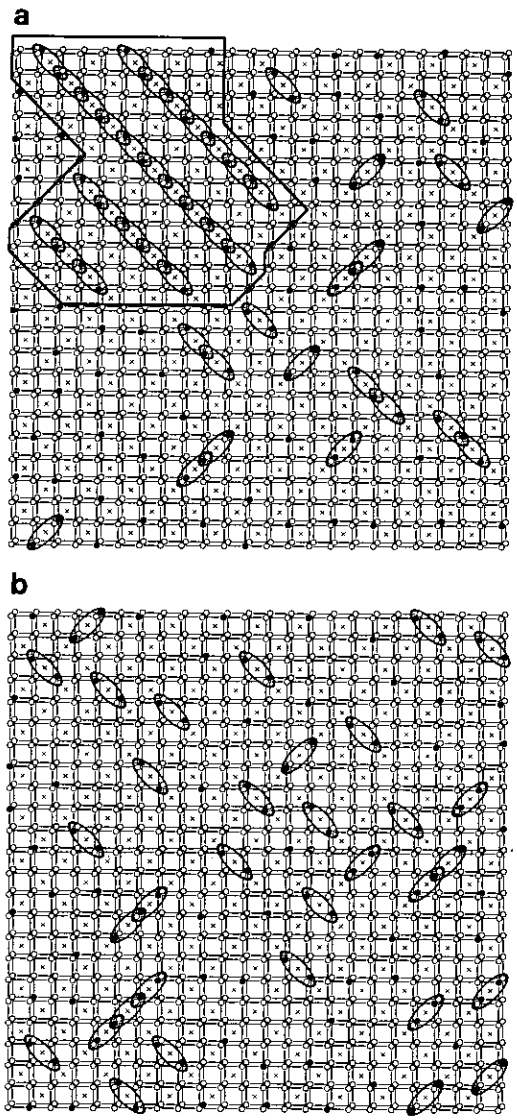

FIG. 6. A small portion of two consecutive layers of the 3D distrbution of oxygen vacancies for the two models described in the text. (a) model 1; (b) model 2. Ellipses are drawn to indicate third-nearest-neighbour $\frac{1}{2}\langle 1\ 1\ 1\rangle$ vacancy pairs, which essentially provide the included cation (indicated by a cross, ×) with octahedral coordination. In model 1 a microcrystal of a pyrochlore-like structure can be seen (outlined).

that the chains of vacancies that occur in the indicated regions are seen to zigzag up and down between the two layers, in a manner analogous to that in the pyrochlore structure (see Fig. 7).

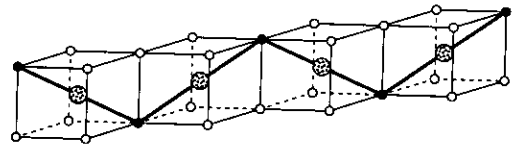

FIG. 7. Schematic drawing showing the zigzag chains of vacancies along $\langle 1\ 1\ 0\rangle$ in the pyrochlore structure.

The relaxation of the cation positions was carried out using essentially the same algorithm used for the 2D simulations. The distance between any two cation sites was assumed to increase to above the average if either of the two bridging oxygen sites was vacant, or correspondingly decrease if both were filled. This was achieved via Monte Carlo simulation using harmonic (Hooke's law) potentials of the form $E = k(d - d_0)^2$, where d_0 was $\sim 1.12\times$ the average intercation vector when a vacancy occurred in the bridging oxygens and $\sim 0.97\times$ the average intercation vector when no vacancy occurred. The ~12% increase compared to ~3% decrease is to take account of the fact that the ratio of cation pairs including a vacancy to pairs with no vacancy is approximately 1 : 4.

Fifty cycles of Monte Carlo iteration were found sufficient to obtain a degree of relaxation close to equilibrium, and this number of cycles was used in all the examples in this paper.

Some sections of the 3D diffraction pattern obtained from this example are shown in Figs. 8a–8c. These are the $0.5c^*$, $0.1c^*$, and h,k,l, $(h + k + l) = 0.5$ sections, corresponding to the observed sections shown in Fig. 1. These patterns were calculated using only the relaxed cation positions and using a single cation scattering factor (Zr) for all the cations.

These diffraction patterns show a number of promising features:

(i) The dark lines occur in the right places.

(ii) There are diffuse peaks in the vicinity of the $\mathbf{G} + \frac{1}{2}(1\ 1\ 1)^*$ reciprocal positions, where $\mathbf{G}$ is a reciprocal lattice vector.

(iii) These diffuse peaks are split in two

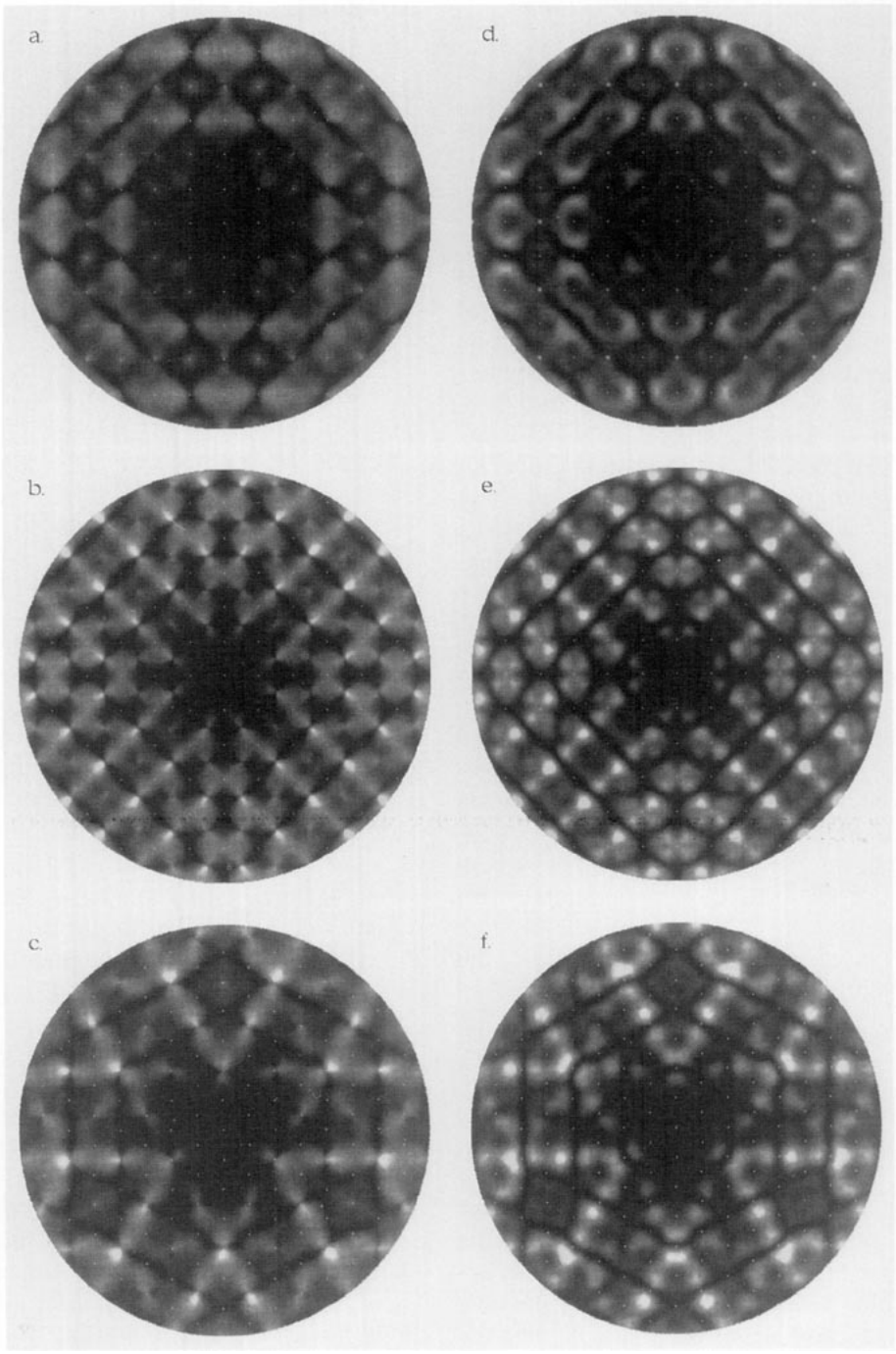

FIG. 8. Calculated diffraction patterns for the two 3D models described in the text. (a, b, c) are from model 1; (d, e, f) are from model 2. The sections are: (a, d), h,k, 0.1; (b,e), h,k, 0.5; (c, f), h,k,l $(h + k + l) = 0.5$. The small white dots mark the positions of integral reciprocal lattice positions in the corresponding zero-level section.

by the dark lines, giving the appearance of pairs of peaks straddling the lines.

(iv) The intensity on the high-angle side of the dark lines is greater than that on the low-angle side.

There are however some features which are evidently quite wrong:

(i) The pairs of split peaks are too close to the dark lines, pinching into the dark lines and giving them a wavy appearance. The experimental dark lines are much straighter and the peaks more clearly separated from the line.

(ii) The central horizontal and vertical intensity minima (i.e., along $k = 0$ and along $h = 0$), which are clearly visible in all c^* sections in the experimental data, are entirely missing.

The clue to the way in which these two incorrect features can be rectified is given by the 2D example of Fig. 3c where both the clearly separated pairs of peaks and the central horizontal and vertical intensity minima are present. In this 2D case these effects were achieved by decreasing the second-neighbor interaction along **v** (i.e., more negative correlation), thereby essentially reducing the length of the pyrochlore-like chains of vacancies. In 3D the length of the pyrochlore-like chains clearly visible in Fig. 6a can correspondingly be reduced by including an interaction between oxygen sites separated by ⟨1 1 0⟩. In the second example, shown in Fig. 6b, the correlation along this vector has been decreased to zero. This example was one of a series carried out in which it was attempted to obtain a value for the ⟨1 1 0⟩ correlations varying between the value of 0.177 of model 1 to a value approaching −0.108 (the maximum possible negative correlation) while maintaining the same value for the ½⟨1 1 1⟩ correlations. However, it was apparent that negative values could only be achieved at the expense of a reduction in the ½⟨111⟩ correlations, and the example shown as model 2 represents something close to the limit of what can be achieved, given the need to maintain the value of the ½⟨1 1 1⟩ correlations.

TABLE III

THE FREQUENCIES WITH WHICH A VACANCY IS SURROUNDED BY 0, 1, 2, 3, OR 4 OTHER VACANCIES AT A DISTANCE OF ½⟨1 1 1⟩

	Number of surrounding vacancies				
Model	0	1	2	3	4
Model 1	0.16	0.31	0.29	0.16	0.07
Model 2	0.0	0.39	0.60	0.01	0.0

The plot of two layers of this example in Fig. 6b shows a preponderance of isolated vacancy pairs with the occasional short chain of two or three zigzag units. This picture is somewhat misleading since a vacancy pair within these two layers can continue as an out-of-plane chain either to the layer above or to the layer below. A truer picture is revealed if we make a count over the whole 3D lattice of the number of times a vacancy occurs with a single, two, three, or more ½⟨1 1 1⟩ neighboring vacancies. In the perfect ordered pyrochlore structure a given vacancy always has four ½⟨1 1 1⟩ neighboring vacancies. In Table III we show the statistics corresponding to the two models shown in Fig. 6. Note that in model 2 there are no isolated vacancies and very few chains longer than two units.

Diffraction patterns corresponding to model 2 are shown in Figs. 8d–8f. Figs. 8e and 8f in particular are now seen to be qualitatively in good agreement with the observed data shown in Fig. 1. The two features which were unsatisfactory in model 1 are now much more satisfactorily modeled. Figure 8d, though in better agreement than Figure 8a, since the minimum of intensity along the k = 0 and h = 0 lines is better modeled, is deficient in that the scattering close to the (0 4 0) and (4 0 0) Bragg positions is missing entirely, at points indicated by the arrows in Fig. 1a. Note, we might also expect to see similar features near (0 2 0) and (2 0 0) but the experimental in-

tensities here have been drastically reduced by absorption. We believe this scattering, which represents the very narrow part of the bow-tie features discussed earlier, that are also visible on sections $0.2c^*$, $0.3c^*$, and $0.4c^*$ (see Ref. (*1*)), originates from the oxygen array, which at present is not included in our scattering model.

The main reason for our belief that this scattering originates from displacements of the oxygen array, whether directly or indirectly (as the result of the constraint it provides to the movement of the cations), is as follows. The lattice parameter of cubic zirconia is such that the mean oxygen–oxygen separation is close to the normally expected minimum interatomic distance (~2.5 Å). Consequently any local relaxation of the oxygen atoms which accompanies the cation relaxations would also be subject to the constraint that this minimum distance be maintained. The result of this is that oxygen motion is likely to be of the "string-pulling" mode type in which rows of oxygen along ⟨1 0 0⟩ directions move in concert. Such motion gives rise to planes of scattering normal to the chains, and occurs most strongly in planes passing through the (0 2 0), (0 4 0), (2 0 0), and (4 0 0) Bragg positions.

4. Conclusion

Although the ultimate aim of the present work was to obtain a fully 3D model of the sructure of cubic-stabilized zirconias which would explain all of the observed features of the diffuse X-ray scattering patterns, the 2D single layer model described in section 2 played a crucial role in its development. This 2D model was very much simpler, computationally less expensive and quicker to use, than a 3D model, but nevertheless contained the essential elements of the problem that could eventually be incorporated into a 3D model. These essential elements were:

(i) That the dark lines observed in the diffraction patterns come from the correlated motion of cations along ⟨1 1 0⟩ directions, resulting from *size-effect*-like differences in length of intercation vectors.

(ii) That the simple mechanism by which this distortion arises is one in which two cations move apart if one or other of the bridging oxygen atoms is missing. Note that in 3D a vacancy will thus affect the *four* cations surrounding it. These will locally move out from the vacancy along ⟨1 1 1⟩ but the effect of this motion will then be transmitted along the ⟨1 1 0⟩ rows of cations as noted in (i).

(iii) That the diffuse spots arise from short-range ordering of the vacancies (and hence presumably the cations). Without the resulting distortion field this short-range ordering would not be detectable in Y-CSZ, as the scattering contrast between Y and Zr is minimal.

(iv) That the asymmetry in the intensity of these spots across the dark planes arises naturally from the distortion model (ii). The detailed mechanism for this is discussed elsewhere (*7*) but in simple terms it may be considered to arise because there are more shorter-than-average intercation vectors and fewer longer-than-average ones.

The 3D model described in section 3 which was developed as a result of extensive investigation of the 2D model provides a simple explanation of virtually all the features that occur in the complex diffuse X-ray diffraction patterns of a cubic-stabilized zirconia. As for the 2D case the 3D model consists of two parts: a scheme for the ordering of oxygen vacancies, followed by the relaxation of cations around these vacancies. The version of the model (model 2) which at present best fits the observed scattering patterns is one in which the oxygen vacancies order in such a way as to avoid nearest-neighbor $\frac{1}{2}\langle 1\ 0\ 0\rangle$ pairs, next-nearest $\frac{1}{2}\langle 1\ 1\ 0\rangle$ pairs and third-nearest $\frac{1}{2}\langle 1\ 1\ 1\rangle$ pairs across empty cubes of oxygens, but allows third-nearest $\frac{1}{2}\langle 1\ 1\ 1\rangle$ pairs across cubes of oxygens containing the cations. These vacancy-pairs which essentially provide octahedral coordination of the enclosed cation are therefore present almost entirely as ei-

ther single isolated octahedra or neighboring ⟨1 1 0⟩ pairs of octahedra. The tendency for such vacancy pairs to form chains as in the pyrochlore structure is avoided as far as possible.

At this stage it is important to note that in all the known fluorite-related superstructure phases (with the one exception of the C-type rare-earth oxide structures which correspond to 25% oxygen vacancies) all anion vacancies occur in pairs separated by $\frac{1}{2}\langle 1\ 1\ 1\rangle$ with a cation in between (*8*). These cation/vacancy pair units may be isolated (as in M_7O_{13}), in linear chains (as in M_7O_{12}), linked into zig-zag chains (as in the pyrochlore structure), helical chains (as in $Ca_6Hf_{19}O_{44}$) or into clusters (as in $CaZr_4O_9$). Furthermore, cation ordering in these superstructure phases is usually linked to the oxygen vacancy ordering in that it is the smallest available cation that is octahedrally coordinated.

The calculated scattered intensity patterns shown in the paper are derived entirely from the cation displacements, and do not include contributions from either the contrast between the two types of cation or from the oxygen atoms. This is clearly a good approximation for the yttria-stabilized material, but for the calcia-stabilized material the contrast between Ca and Zr needs to be included. For example the transfer of intensity across the dark lines which is so characteristic and consistent in the yttria, is sometimes in the opposite direction for the calcia. Nevertheless, the fact that the dark lines are still visible in the calcia, and that the patterns of the two are very similar, strongly indicates that for the calcia-stabilized material too the major part of the scattering originates from the cation displacements, induced by relaxation around a similar distribution of oxygen vacancies. The particular calcia-stabilized material for which we have recorded data (shown in Fig. 1) has an oxygen vacancy concentration only approximately half of that in the yttria material. It is possible that the extra sharpness of the diffuse peaks in the calcia material arises because of the extra freedom that the fewer vacancies have to avoid each other, rather than being a property of the particular cation. Work is in progress to investigate materials of different compositions in both the yttria- and the calcia-stabilized series.

Although the diffraction patterns calculated from the present model cannot be said to be in fully *quantitative* agreement with experiment, we believe that the model has all the essential features *qualitatively* correct. The model also has the advantage that it is simple and consistent with known fluorite-related superstructure phases. In respect of the magnitude of the local intercation displacements we believe that the asymmetry across the dark lines that is observed, unequivocally requires that root mean square atomic displacements of ~3% must be present (*7*). In its present form the model is capable of further refinement so that a better match to experiment might be obtained by small adjustments of either the vacancy ordering procedure or the cation relaxation scheme. Perhaps of more importance, though, is the necessity to incorporate into the model the oxygen atom displacements and the distribution of the two types of cation.

In the present model 2 ~38% of the cation sites have [8]-fold coordination, ~46% have [7]-fold coordination and ~16% have [6]-fold coordination. Since it is known that zirconium is able to tolerate a whole range of different coordination environments and in particular is frequently found in [7]-fold sites (*9*), a particularly simple solution to the question of how to distribute the two species of cation would be to place the Y atoms (~39% of the cations) in the [8]-fold sites and the Zr atoms in the [6] and [7] sites. Such an ordering scheme is not required by the diffraction data but would be in accord with known fluorite-related superstructures in that the [6]-fold sites are invariably occupied by the smallest available cation (in our case the Zr^{4+}) while the [8]-fold sites are usually occupied by the larger cations. In

the case of calcia-stabilized zirconia, the question as to whether anion vacancies are preferentially associated with Zr's or Ca's remains a controversial point. Rossell *et al.* (*10*) argue strongly for the former while Morinaga *et al.* (*11*) on the basis of a fit to measured diffuse data, claim the latter. While the measured diffuse intensity distribution, in the case of the calcia stabilized zirconia (see Fig. 1), is clearly still dominated by displacive effects rather than chemical ordering, there is some indication that effects due to chemical ordering may be present in the data. Further work on this aspect of the problem is in progress.

Following the allocation of cations to the different coordination sites, oxygen atoms could then be placed in each available tetrahedral coordination site, and their positions adjusted iteratively to satisfy bond-valence requirements with the four cations. Any model must not only fit observed diffuse scattering data but also be locally chemically plausible. Calculation of apparent valences (AVs) is a good way of checking for local chemical plausibility. For example the microdomain of type A1 recently reported to occur in calcia-stabilized zirconia (*12*) gives a calculated AV for Ca^{2+} of ~3.7 rather than 2.0 and hence would appear not to be chemically plausible. Similarly, models requiring O–O separation distances less than ~2.5 Å are also chemically implausible. Further systematic work along these lines is being undertaken.

Acknowledgment

The diffuse scattering images shown in Figs. 3 and 8 were computed on a Fujitsu VP-2200 supercomputer using a grant from the Australian National University Supercomputer Facility. We would also like to thank Joseph F. Wenckus, Chairman of Ceres Corporation, for the generous supply of single crystal samples used in this study.

References

1. T. R. Welberry, R. L. Withers, J. G. Thompson, and B. D. Butler, *J. Solid State Chem.* **100,** 71 (1992).
2. B. D. Butler, R. L. Withers, T. R. Welberry, *Acta Crystallogr. Sect. A* **48,**737 (1992).
3. B. D. Butler, and T. R. Welberry, *J. Appl. Crystallogr.* **25,** 391 (1992)
4. T. R. Welberry, and T. N. Zemb, *J. Colloid Interface Sci.* **123,** 413 (1987)
5. B. G. Hyde and S. Andersson, "*Inorganic Crystal Structures,*" Wiley, New York (1989).
6. R. L. Withers, J. G. Thompson, P. J. Barlow, and J. C. Barry, *Aust. J. Chem.* **45,** 1375 (1992).
7. B. D. Butler and T. R. Welberry, *Acta Crystallogr Sect. A***49,** in press (1993).
8. Rossell, H. J. and H. G. Scott, *J. Phys. Colloq.* **38,** C7 (1977).
9. C. J. Howard, R. J. Hill, and B. E. Reichert, *Acta Crystallogr Sect. B***44,** 116 (1988).
10. H. J. Rossell, J. R. Sellar, and I. J. Wilson, *Acta Crystallogr. Sect. B***47,** 862 (1991).
11. M. Morinaga, J. B. Cohen, and J. Faber, Jr., *Acta Crystallogr. Sect. A***36,** 520 (1980).
12. R. B. Neder, F. Frey, and H. Schultz, *Acta Crystallogr., Sect. A***46,** 799 (1990).